High Efficiency Organic Solar Cells Achieved by the Simultaneous Plasmon-Optical and Plasmon-Electrical Effects from Plasmonic Asymmetric Modes of Gold Nanostars

Xingang Ren, Jiaqi Cheng, Shaoqing Zhang, Xinchen Li, Tingke Rao, Lijun Huo, Jianhui Hou, and Wallace C. H. Choy*

The plasmon-optical effects have been utilized to optically enhance active layer absorption in organic solar cells (OSCs). The exploited plasmonic resonances of metal nanomaterials are typically from the fundamental dipole/high-order modes with narrow spectral widths for regional OSC absorption improvement. The conventional broadband absorption enhancement (using plasmonic effects) needs linear-superposition of plasmonic resonances. In this work, through strategic incorporation of gold nanostars (Au NSs) in between hole transport layer (HTL) and active layer, the excited plasmonic asymmetric modes offer a new approach toward broadband enhancement. Remarkably, the improvement is explained by energy transfer of plasmonic asymmetric modes of Au NS. In more detail, after incorporation of Au NSs, the optical power in electron transport layer transfers to active layer for improving OSC absorption, which otherwise will become dissipation or leakage as the role of carrier transport layer is not for photon-absorption induced carrier generation. Moreover, Au NSs simultaneously deliver plasmon-electrical effects which shorten transport path length of the typically low-mobility holes and lengthen that of high-mobility electrons for better balanced carrier collection. Meanwhile, the resistance of HTL is reduced by Au NSs. Consequently, power conversion efficiency of 10.5% has been achieved through cooperatively plasmon-optical and plasmon-electrical effects of Au NSs.

X. G. Ren, J. Q. Cheng, Dr. X. C. Li, T. K. Rao,
Prof. W. C. H. Choy
Department of Electrical and Electronic Engineering
The University of Hong Kong
Pokfulam Road, P. R. China
E-mail: chchoy@eee.hku.hk
S. Q. Zhang, Prof. L. J. Huo, Prof. J. H. Hou
Institute of Chemistry
Chinese Academy of Sciences
Beijing 100190, China

1. Introduction

Recently, plasmon-optical effects of metal nanostructures have been extensively used to boost active layer absorption in organic solar cells (OSCs).[1–9] Typically, the plasmonic resonances of nanomaterials are categorized into surface plasmonic resonance (SPR) of grating structures and localized surface plasmonic resonance (LSPR) of nanoparticles (NPs). The nanostructured electrode with periodic pattern can excite the SPRs as well as waveguide modes to favor

the active layer absorption in OSCs.[10,11] The restoring force induced by the particle's curved surface will produce a strong oscillation of the driven electrons in metal NPs, resulting in the promotion of active layer absorption at LSPRs by the highly concentrated near fields and strong scattering.[12–17]

The incorporation of metal NPs in active layer, electron transport layer (ETL), and hole transport layer (HTL) can improve active layer absorption while their enhancement mechanisms are totally different. The large field intensity in active layer due to the excitations of fundamental dipole and high-order modes of the embedded metal NPs mainly contributes to absorption enhancement of active layer.[13,14,18–20] For metal NPs embedded into carrier transport layer (ETL and HTL), the achieved absorption enhancement is attributed to the elongated optical path length caused by the plasmonic enhanced scattering effects of metal NPs.[15–17,21]

The fundamental dipole or high-order modes of plasmonic metal NPs are typically narrow bandwidth resulting in a regional OSC absorption enhancement. To achieve the broadband enhancement covering the whole visible region, it needs a linear superposition of resonances through the simultaneous incorporation of different type metal nanomaterials (i.e., with different material species, shapes, sizes etc.) in an OSC at the same time.[4,13,16,21,22] Consequently, it is highly desirable to have a simple and efficient way to obtain the broadband enhancement of active layer absorption.

Besides the aforementioned plasmon-optical effects of plasmonic metal nanomaterials, the concomitant plasmon-electrical effects have been found to be helpful in improving OSC electrical properties such as carrier transport and collection. In previous reports, the incorporation of metal NPs into OSCs were reported to ameliorate the morphologies, device conductivities and carrier mobilities.[23–25] Moreover, the better carriers' (electron and hole) extraction can also be achieved through manipulating exciton generation regions, i.e., carrier transport path length, especially for charge carriers with severely imbalanced mobilities.[26,27] Through the incorporation of metal NPs in the region of active layer near to anode, the exciton generation regions will be relocated close to the anode.[27] Therefore, the transport path length of the typically low-mobility holes will be shortened and that of high-mobility electrons will be lengthened for achieving the balanced and improved collection of carriers. It is of great interest to improve carrier collection by plasmon-electrical effects through introducing a new type of metal NPs at the interfacial regions of active layer and carrier transport layer.

The employment of metal nanomaterials with complex geometry can provide broadband resonances due to the inherent coupling between its core and protuberant spines.[28–32] The highly concentrated field intensity around the branched corners and edges offered by the metal nanostars (NSs) together with the remarkable scattering are of great potential to enhance active layer absorption. To achieve a broadband absorption enhancement, the utilization of metal NSs would be much simple as compared to the conventionally simultaneous usage of different metal NPs in OSCs. However, the metal NSs embedded OSCs have been rarely studied.[31] Moreover, the incorporation of metal NSs in OSCs simultaneously penetrating into both active layer

and carrier transport layer are not comprehensively investigated. Therefore, it is highly desirable to understand the uniquely plasmon-optical and plasmon-electrical effects by the plasmonic metal NSs when they are incorporated in between active layer and carrier transport layer in OSCs.

In this work, we incorporate the gold (Au) NSs in between HTL and active layer to comprehensively survey the role of Au NSs in improving OSCs efficiency. Our results demonstrate that the excitations of plasmonic asymmetric modes of Au NSs (that embedded in HTL and simultaneously penetrated into active layer) can provide broadband resonances and OSC absorption enhancement which are distinct from the conventional linear superposition of fundamental dipole and high-order resonances of several metal NPs. We find that the broadband enhancement can be explained by the energy transfer induced by the embedded Au NSs. To be more specific, after the incorporation of Au NSs, the optical power in ETL will transfer to active layer and then contribute to the improvement of active layer absorption. Otherwise, the energy at ETL will be the waste in terms of dissipation or leakage as the role of carrier transport layer is not for photon-absorption induced carrier generation. Therefore, the enhancement of optical absorption can be achieved over the broadband wavelength regions (350–750 nm). In addition, the theoretical and experimental results demonstrate plasmon-electrical effects generated by the incorporated Au NSs improve the electrical properties of both the active layer and HTL in OSCs. It not only facilitates the carrier transport in active layer (owing to the balanced and improved collection of carriers as described above) but also improve the hole transport properties from active layer to electrode through HTL (due to the considerable reduction of the transport resistance). Consequently, the power conversion efficiency (PCE) up to 10.5% can be achieved for the Au NS incorporated OSCs.

2. Results and Discussion

2.1. Device Performances

The highly efficient benzodithiophene (BDT)-thieno[3,4-b]thiophene backbone-based polymer (PBDT-TS1) with the broadband extinction coefficient (see Figure S1, Supporting Information) is adopted as the polymer donor and poly(3,4-ethylenedioxythiophene): poly(styrene sulfonate) (PEDOT:PSS) is used as HTL which has good energy level alignment with PBDT-TS1:[6,6]-phenyl C71-butyric acid methyl ester (PC$_{71}$BM). We have fabricated the control OSC with a structure of glass/indium tin oxide (ITO)/PEDOT:PSS (30 nm)/PBDT-TS1:PC$_{71}$BM (90 nm)/calcium (Ca, 20 nm)/ aluminum (Al, 100 nm). The Au NSs are well dispersed into PEDOT:PSS solutions to form Au NS incorporated OSC as shown in **Figure 1**a. The Au NS synthesis, device fabrication and characterization are described in *Experimental section*. The Au NSs with sizes around 70 nm are characterized with transmission electron microscopy (TEM) in the inset of Figure 1b. The film of the PEDOT:PSS doped with Au NSs was formed by spin coating and the randomly distributed Au
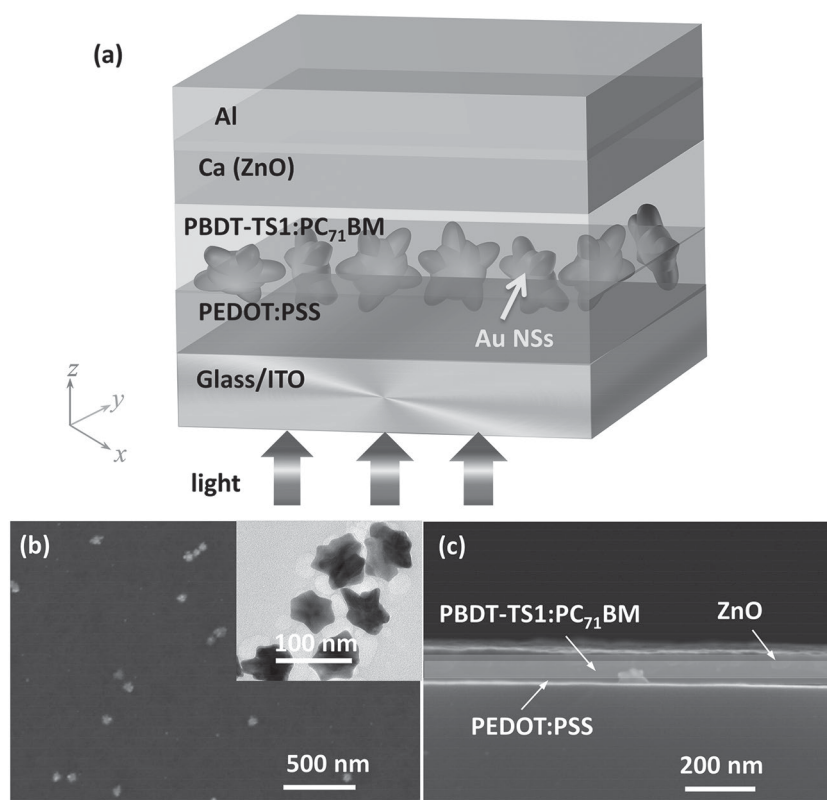
Figure 1. a) The schematic illustration of the structure of Au NS incorporated OSC. b) The top view of the spin-coated PEDOT:PSS film doped with Au NSs on ITO substrate. The inset is the TEM image of the Au NSs with sizes of 70 nm. c) The cross-sectional view of the film with Au NS incorporated in PEDOT:PSS and PBDT-TS1:PC$_{71}$BM layer. The white scale bars are 500 nm (inset 100 nm) in (b) and 200 nm in (c).

NSs are clearly observed in Figure 1b. Since the thickness of the spin-coated PEDOT:PSS film (2000 rpm for 60 s) is around 30 nm, Au NSs with average sizes of 70 nm are penetrated into active layer, i.e., Au NSs are located in between PEDOT:PSS and PBDT-TS1:PC$_{71}$BM layer (see Figure 1c). As shown in Figure S2 (Supporting Information), the atomic-force microscopy image reveals that there are no clear changes of the top surface roughness of active layer after the incorporation of Au NSs. The optimized concentration of Au NSs in OSC is 1 mg mL^{-1}. The further increment of Au NSs concentrations would be detrimental to the active layer morphology and also introduce a significant device reflection loss.

The current density–voltage (J–V) curves of OSCs are measured as shown in **Figure 2**a. With the incorporation of Au NSs, the short-circuit current density (J$_{SC}$) increases to 18.72 from 17.08 mA cm^{-2} (control). The device performances are detailed in **Table 1** (averaged over ten devices). PCE increases to 10.25% from 9.26%. After further replacement of ETL Ca by zinc oxide (ZnO), PCE reaches 10.5% (average) due to the further increment of J$_{SC}$ to 19.24 mA cm^{-2}. The incident

photon-to-current conversion efficiency (IPCE) spectra also reveal a conspicuous improvement over the visible region especially from 350 to 750 nm (see Figure 2b). The optical path length in active layer has been elongated due to the scattering from the portion of Au NSs in HTL. Meanwhile, the remaining portion of Au NSs (about 40 nm in size) penetrated into active layer directly promote optical absorption owing to the highly confined near field. The multiple optical effects (i.e., the scattering and highly confined near field) cooperatively improve the active layer absorption over such wideband region and offer a prominent J$_{SC}$ increment. It can be observed that there are two distinct peaks (around 350 and 520 nm represented by peaks 1 and 2) in IPCE enhancement spectra (denoted as ΔIPCE) as shown in Figure 2b which are far away from the fundamental dipole resonance of Au NSs (around 700 nm). The plasmon-optical effects contribute to the IPCE enhancement will be described in details in the next sections.

2.2. Optical Effects

To study the underlying mechanisms of the two distinct peaks (around 350 and 520 nm represented by peaks 1 and 2 in Figure 2b) in the broadband ΔIPCE spectra, Maxwell's equations for the 3D OSC model are rigorously solved using the finite-difference time-domain (FDTD) method.[33,34] In our model, the Au NSs are modeled by a solid sphere core with several branched spines. The resonances of the Au NSs in water solutions obtained by the numerical FDTD method are comparable with that of the experimental measurement (see Figure S3a, Supporting Information). The fundamental dipole mode of Au NSs contributes to absorption enhancement at the wavelength around 700 nm through plasmon-optical
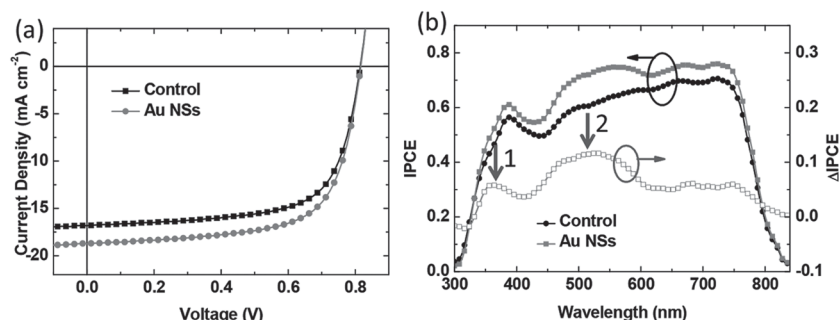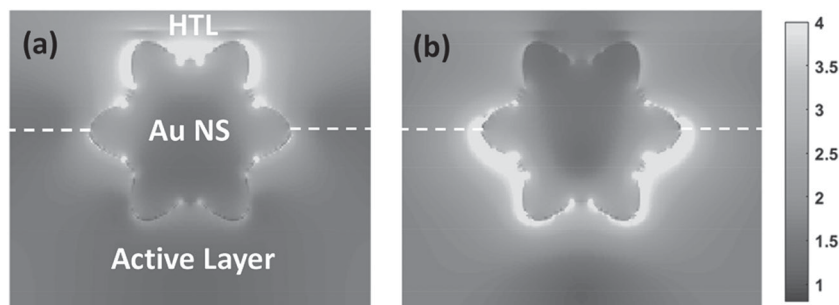

Figure 2. a) The current density–voltage (J–V) curves and b) incident photon-to-current conversion efficiency (IPCE) of the device with structure of ITO/PEDOT:PSS (w/wo Au NSs)/PBDT-TS1:PC$_{71}$BM/Ca/Al. The improvement of IPCE is denoted as ΔIPCE and the peaks 1 and 2 are due to the excitations of plasmonic asymmetric modes by the incorporated Au NSs.

Table 1. The summary of photovoltaic characteristics of control and Au NS incorporated OSCs (averaged over ten devices).

Device	V_{OC} [V]	J_{SC} [mA cm^{-2}]	FF [%]	PCE [%]
PBDT-TS1				
Control	0.81 ± 0.01	17.08 ± 0.21	66.89 ± 0.23	9.26 ± 0.09
Au NSs	0.81 ± 0.01	18.72 ± 0.26	67.66 ± 0.26	10.25 ± 0.11
Control (ZnO)	0.81 ± 0.01	18.37 ± 0.20	67.00 ± 0.21	9.97 ± 0.08
Au NSs/ZnO	0.81 ± 0.01	19.24 ± 0.25	67.70 ± 0.24	10.50 ± 0.10

effects. Since Au NSs are embedded in between PEDOT:PSS (HTL, $n \approx 1.5$) and PBDT-TS1:PC$_{71}$BM (active layer, $n \approx 1.9$), the high-order resonance of Au NSs will be excited and split into two resonances due to the asymmetric dielectric environment. The plasmonic asymmetric high-order modes will increase the local density of states around Au NSs and then significantly boost the active layer absorption leading to the two distinct peaks at 350 and 520 nm in IPCE enhancement (i.e., ΔIPCE) spectra. To verify this statement, we have calculated the optical absorption of the incorporated Au NS in OSCs. There are two corresponding absorption peaks (located around 340 and 560 nm as shown in Figure S3b, Supporting Information) which confirm the plasmonic asymmetric high-order plasmonic resonance modes of Au NS. Meanwhile, as shown in **Figure 3**, the excited plasmonic asymmetric modes by Au NSs can be further recognized by the asymmetric near field distributions as compared to that of the fundamental symmetric dipole mode (Figure S4, Supporting Information). The protuberant spines of Au NS incorporated in HTL will induce the strongly localized near-field distributions (Figure 3a) that contribute to the emergence of peak 1 in ΔIPCE spectra. It should be noted that the plasmonic asymmetric modes enhanced scattering and prolonged light path in active layer are the in-depth reasons for the enhancement at wavelength 340 nm. Correspondingly, the near-field distributions in Figure 3b unveil that the plasmonic resonance of the Au NS spines in active layer is attributed to peak 2 in ΔIPCE spectra. As a consequence, the excitations of the plasmonic asymmetric high-order modes by the Au NSs in between HTL and active layer as well as the fundamental dipole mode resonance produce a considerable enhancement over a broadband region.

Interestingly, we found the plasmonic asymmetric modes of Au NSs can manipulate the optical-power distribution via energy transfer which is distinct from the modulation of electrical field intensity through utilizing optical spacer (i.e., optimization of electric field distribution in active layer through precisely tuning the spacer thickness). As shown in **Figure 4**a, the distributions of absorptive power in each stacked layer of control OSC (without Au NSs) are calculated. The absorbed optical power in active layer reveals several hot spots corresponding to the peaks in extinction coefficient spectra of PBDT-TS1:PC$_{71}$BM (Figure S1, Supporting Information). After the incorporation of Au NSs in between HTL and active layer, the absorptive power increases in PEDOT:PSS and active layer (not shown), the variation of the absorptive power is shown in Figure 4b. It clearly reveals two hot spots in active layer (i.e., increment of absorptive power) around the wavelengths of 340 and 560 nm that are consistent with the peaks in ΔIPCE spectra. Besides, it is noteworthy that there are two corresponding dark regions in Ca layer (i.e., reduction of absorptive power) which indicates the existence of optical power redistribution in Ca and active layer. In other words, through the strategic incorporation of Au NSs, the optical power previously dissipated in Ca will transfer to active layer then contribute to the improvement of active layer absorption. Therefore, the energy transfer between Ca and active layer are the in-depth reason for such increment of J_{SC} in Au NS incorporated OSC.

However, the metal loss of Ca is still large and may hinder the total light absorption by the active layer while low loss ETL such as ZnO can further improve the active layer absorption.[35–37] By using ZnO, the position-dependent absorptive power demonstrates metal loss of Ca can be significantly reduced. (see Figure S5, Supporting Information) As shown in Figure S5b, the variation of the absorbed optical power in active layer reveals two hotspots which indicate the existence of energy transfer by the plasmonic asymmetric modes of Au NSs. The optical power in ZnO transfers to active layer and contributes to photocurrent improvement (otherwise will become waste in terms of leakage or radiation loss). The J–V curves and IPCE spectra of the ZnO-based OSCs are shown in Figure S6 (Supporting Information). The two peaks (350 and 520 nm) induced by the plasmonic asymmetric modes exist in the ΔIPCE spectra of OSCs with Au NSs and ZnO ETL. Finally, a very high PCE up to 10.5% and J_{SC} of 19.24 mA cm^{-2} have been achieved (See Table 1).

To reconfirm the enhancement, the OSCs with polythieno[3,4-b]-thiophene-*co*-benzodithiophene (PTB7):PC$_{71}$BM have also fabricated with the same device structure. The J–V curves are shown in Figure S7 (Supporting Information) (Detailed device performances are listed in Table S1, Supporting Information). With Au NSs in between PEDOT:PSS and PTB7:PC$_{71}$BM, the PCE increases to 9.34% from 8.77% (optimized control). The PCE can be further improved to 9.71% (average) with ZnO as

Figure 3. The near-field intensity distributions of Au NS incorporated in between HTL and the active layer. The asymmetric high-order modes of Au NS are excited in a) HTL and b) active layer which corresponds to peaks 1 and 2, respectively, as indicated in ΔIPCE spectra in Figure 2b. The white dash lines represent the interface between HTL and active layer.
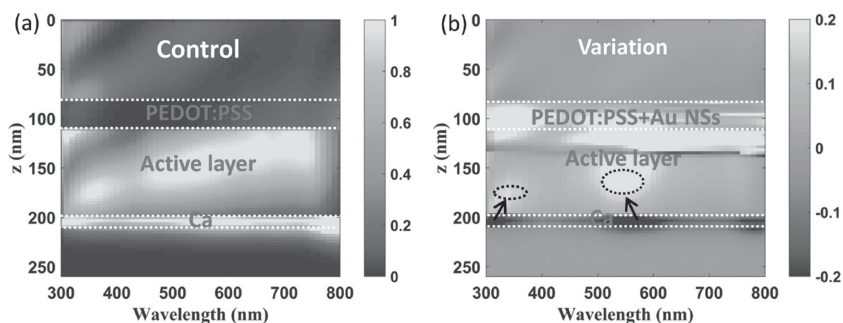
Figure 4. a) The absorptive power distributions of the control OSC (without Au NSs). The absorptive power in Ca cannot contribute to the carrier generation and would be waste. b) The variation of absorptive power distribution due to the incorporation of Au NSs compared to the control OSC. Due to the excitation of plasmonic asymmetric modes, the absorptive power in Ca would transfer to active layer and contribute to photon-absorption induced carrier generations. The black arrows represent the direction of energy transfer from Ca to active layer and the enhancement regions are indicated by circular black dotted regions, i.e., at the wavelength around 340 and 560 nm. The regions of each layer are indicated by white dotted lines. The absorptive power is calculated by the formulae: $P = -1/2\omega \operatorname{Im}\{\varepsilon\}|E|^2$ and then integrated over xoy plane, where ω is angular frequency, $\operatorname{Im}\{\varepsilon\}$ is imaginary part of active layer permittivity and E is electric field.

ETL due to the increment of J_{SC} up to 18.05 mA cm^{-2}. Consequently, the incorporation of Au NSs in between HTL and active layer is a universal strategy to boost OSC efficiency through the excitation of plasmonic asymmetric modes.

2.3. Electrical Effects

Besides the absorption enhancement induced by plasmon-optical effects of the incorporated plasmonic Au NSs, we find that the concomitant plasmon-electrical effects also contribute to the OSC efficiency improvement. Importantly, the incorporated Au NSs favor a more balanced and improved carrier collection through manipulating the carrier transport length (i.e., plasmon-electrical effects). The electron and hole mobilities are determined by J–V characteristics of the electron- and hole-only devices, respectively, using the space charge limited current model[38–40] (Figure S8, Supporting Information). The electron mobility of active layer PBDT-TS1:PC$_{71}$BM is 6.56×10^{-2} cm^2 v^{-1} s^{-1} which is one order magnitude larger than hole mobility 1.18×10^{-3} cm^2 v^{-1} s^{-1}. Therefore, electrons will quickly transport to ETL and collected by the cathode, while holes will slowly transport to HTL and some will accumulate in OSC. In the proposed device, the strategic incorporation of Au NSs in between HTL and active layer can reallocate the exciton generation regions to around HTL side. Under this situation, the transport path length of typically low-mobility holes to anode can be shortened while the transport path of high-mobility electrons to cathode is lengthened for achieving a better carrier collection.

For the control OSC without Au NSs, the exciton generation rates are evenly distributed along the active layer region as shown in Figure S9 (Supporting Information). After incorporating Au NSs in OSCs, the exciton generation regions reveal the substantial modifications. For Au NS incorporated in active layer (PBDT-TS1:PC$_{71}$BM) only, the exciton generation regions are concentrated around Au NSs in the middle of active layer region due to the excitation of dipole mode (**Figure 5**a). Differently, when Au NSs are incorporated in between HTL (PEDOT:PSS) and active layer, the exciton generation regions are reallocated to around HTL region, i.e., near anode (Figure 5b) leading to a short transport path length to anode for low-mobility holes. Importantly, the exciton generation rate of OSC with Au NSs in between HTL and active layer is relatively higher than Au NSs in active layer only (see Figure 5) owing to the excitation of the plasmonic asymmetric modes. With the higher exciton generation rate and better transportation of low-mobility hole to HTL, the fill factor (FF) of Au NS incorporated OSC is increased to 67.66% from 66.89%. (See Table 1) Moreover, we have extracted the experimental absorption (1 – reflection (R) – transmission (T) – parasitic absorption (A0)) to evaluate the internal quantum efficiency (IQE).[41] As shown in Figure S10 (Supporting Information), IQE spectra reveal a conspicuous enhancement after the incorporation of Au NSs indicating the improved OSC electrical properties. Consequently, through the strategic incorporation of Au NSs in between HTL and active layer, the better extractions of photogenerated electrons and holes from active layer to electrode and concomitantly enhanced device performances have been achieved by plasmon-electrical effects.

To further study the improvement of electrical properties, the impedance spectroscopy (IS), a powerful technique to obtain the information about resistance properties of interface and carrier dynamics in the device is also adopted
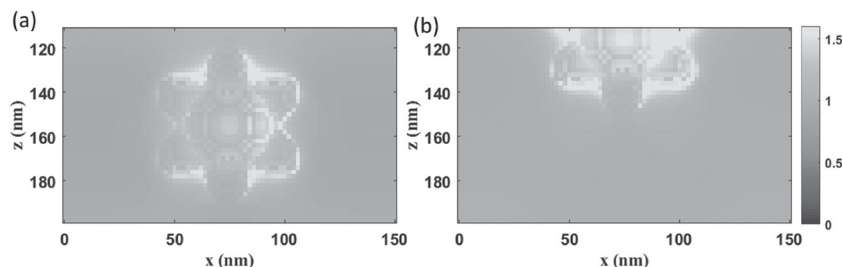

Figure 5. The enhancement of exciton generation rates in active layer with Au NS incorporated a) in active layer (PBDT-TS1:PC$_{71}$BM) only and b) in between HTL (PEDOT:PSS) and active layer compared to control OSC (without Au NS). In the calculation of exciton generation rate, the absorption of Au NS has been excluded and the distribution of exciton generation rate is then integrated over y-axis. The enhancement in (a) is due to the excitation of fundamental dipole mode. The excitation of plasmonic asymmetric modes in (b) shifts the exciton generation regions to near HTL side.
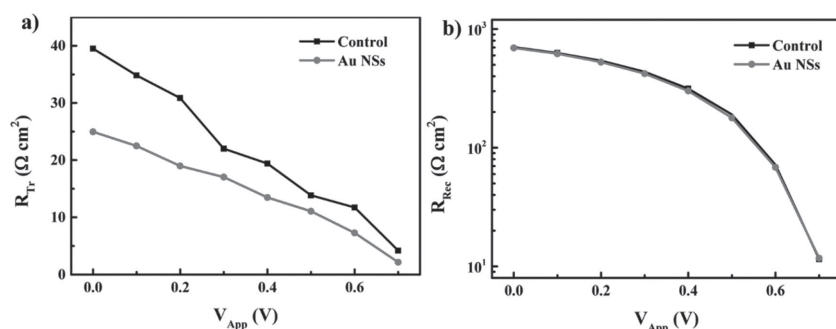
Figure 6. The experimental impedance spectroscopy. a) The extracted transport resistance and b) recombination resistance for the control and Au NS incorporated OSCs.

to investigate the properties of carrier extraction. Through superimposing a small voltage signal on a DC voltage, the carrier transport and recombination mechanisms can be identified by analyzing the frequency response of the electrical impedance. The influence from the incorporation of Au NSs in between HTL and active layer (with Ca as ETL) on OSC electrical properties is captured by IS spectra in Figure S11a (Supporting Information). As we known, the main arc of Nyquist plot at low frequency is related to the recombination process and the arc at high frequency is attributed to the hole transport properties.[42,43] Based on the equivalent circuit described in inset of Figure S11a (Supporting Information), the transport and recombination resistances have been quantitatively extracted from the Bode plot, respectively. As shown in **Figure 6**a, the transport resistance has been remarkably reduced after the incorporation of Au NSs. The hole transport properties from active layer to electrode through HTL can be significantly improved due to the plasmonic excited hot carriers of the incorporated Au NSs.[44–46] As the applied voltage approaching to the open circuit voltage, the improvement of transport resistance becomes weak since all the electrons and holes are recombined under open circuit condition. However, there is no difference in recombination resistance for the control and Au NS incorporated OSCs indicating that the embedded Au NSs do not introduce clear recombination losses. (Figure 6b) As a result, the simultaneous achievement of the better balanced extraction of electrons and holes from active layer to electrode as well as the enhancement of transport properties in HTL cooperatively improves the electrical properties of Au NS incorporated OSC.

3. Conclusion

In conclusion, in this work, we demonstrate that the incorporation of Au NSs in between HTL and active layer generates a broadband absorption enhancement through excitations of plasmonic asymmetric modes. The plasmonic asymmetric modes induce two distinct peaks at 350 and 520 nm in ΔIPCE spectra which is confirmed by the absorption spectra of the embedded Au NSs and corresponding near-field distribution. We find that the plasmonic asymmetric modes of Au NSs can transfer the optical power in ETL (which otherwise will be waste as the role of carrier transport layer is not for photon-absorption induced carrier generation) to active layer and

thus improves the active layer absorption. At the same time, the plasmon-electrical effects are obtained in OSC which favor a more balanced of photogenerated electrons and holes from active layer to electrode as well as reduce transport resistance in HTL, respectively. The synergetic plasmon-optical and plasmon-electrical effects push the PCE up to 10.5% for OSCs with Au NSs and ZnO as ETL. The comprehensive understanding of the role of Au NSs in OSCs would be of great use to further understanding of the plasmonic enhanced OSCs.

4. Experimental Section

Synthesis of Gold Nanostars (Au NSs): The seed solution of the Au NSs was prepared as following. The small gold colloid is synthesized via traditional method.[47] First, 0.6 mL 1 wt% citrate solution is added into 4 mL 1×10^{-3} M $HAuCl_4$ and then boiled for 5 min. After cooling to room temperature, the gold colloid was kept at 4 °C for further use. For the growth of Au nanostars, 2.5 mL of 1×10^{-3} M $HAuCl_4$ solution and 10 μL of 1 M HCl solution were added into 7.5 mL deionized water, then 100 μL previous prepared seed solution was added. The mixture solution is kept stirred under room temperature for one minute. Then 100 μL of 2×10^{-3} M $AgNO_3$ solution and 100 μL of 0.1 M ascorbic acid were added, followed by another 30 s stirring. The color change can be observed soon after ascorbic acid was added. First the solution becomes pink but soon turned into blue color. After 15 min, the growth solution was centrifuged at 6000 rpm for 20 min for two times and dispersed in 1 mL deionized water. The ascorbic acid was used during the synthesis process of Au NS to modify the surface of Au NS with hydroxyl groups. The functional group makes the Au NSs disperse well.

Device Fabrications: The glass/ITO substrates were cleaned with deionized water, acetone, ethanol, and UV-ozone treatment for 15 min. The sheet resistance of the ITO is 15 Ω $\square^{-1}$. The prepared PEDOT:PSS solution at the same concentration with or without Au NSs was spin coated on the ITO substrates at 2000 rpm for 60 s. The optimized concentration of Au NSs is 1 mg mL^{-1}. The PBDT-TS1 (PTB7):PC_{71}BM solution was dissolved in chlorobenzene at the concentration of 10 mg mL^{-1}:15 mg mL^{-1} (with 3% v/v 1,8-diiodooctane additive). The active layers were formed by spin coated the prepared solution to form 90 nm thickness films. ETL of Ca (20 nm) was thermally evaporated and ETL of ZnO (20 nm) was spin coated on the active layers as reported previously.[36] The cathode of Al (100 nm) was evaporated with a shadow mask with an area of 0.06 cm^2.

Device Characterization and Measurement: The morphological analysis of Au NSs was taken by scanning electron microscopy Hitachi S-4800. The current density–voltage (*J*–*V*) curves were measured by using a source meter Keithley 2635 of the OSCs under the illumination of an ABET AM 1.5 G solar simulator. The statistical errors of each parameter are sampled at least of ten devices. The IPCE measurement of OSCs was taken by a home-built IPCE measurement system with a Newport xenon lamp, a monochromator, a

preamplifier, and a lock-in amplifier. The impedance spectroscopy results were measured by a computer-controlled potentialstat (Autolab PGSTST320N) from 100 Hz to 1 MHz. A small voltage perturbation (20 mV rms) is applied. Measurements were carried out under 1 sunlight intensity illumination at different DC bias voltage. Resistance and capacitance were extracted by fitting the spectra using the Z-view software.

Theoretical Modeling: The theoretical results of OSCs with and without Au NS are obtained by analytically solving Maxwell's equations in full-scale 3D FDTD simulation. The refractive indices of PBDT-TS1:PC$_{71}$BM, PEDOT:PSS, and ZnO are measured by ellipsometry spectroscopy. To simplify the model and save computational resource and simulation time, we consider that Au NSs are regularly distributed in OSCs. The periodic boundary conditions are applied in horizontal, i.e., xoy plane, the absorbing boundary conditions are adopted on the top and bottom sides, i.e., z-direction. The periodicities in the xoy plane are $Px = Py = 620$ nm (followed the average measured spacing between Au NSs), the height in the z-direction is 400 nm. The mesh size used in simulation is $dx = dy = dz = 2$ nm. The absorptive power is calculated by the formulae: $P = -1/2\omega \, \text{Im}\{\varepsilon\}|E|^2$, where ω is the angular frequency, $\text{Im}\{\varepsilon\}$ is the imaginary part of the active layer permittivity, and E is the electric field. The profile of absorptive power in z-direction versus wavelength is integrated over xoy plane. The exciton generation rate is obtained through integrating the electrical field intensity with the air mass (AM) 1.5G solar spectrum $\Gamma(\lambda)$: $G = \pi/h \int |\text{Im}\{\varepsilon\}|E|^2 \Gamma(\lambda) \, d\lambda$. The 3D region occupied by Au NSs has been excluded before the integration of electric field intensity in active layer.

Supporting Information

Supporting Information is available from the Wiley Online Library or from the author.

Acknowledgements

[1] Q. Q. Gan, F. J. Bartoli, Z. H. Kafafi, *IEEE Photonics J.* **2012**, *4*, 620.
[2] Q. Q. Gan, F. J. Bartoli, Z. H. Kafafi, *Adv. Mater.* **2013**, *25*, 2385.
[3] C.-C. Chueh, M. Crump, A. K. Y. Jen, *Adv. Funct. Mater.* **2016**, *26*, 321.
[4] X. H. Li, X. G. Ren, F. X. Xie, Y. X. Zhang, T. T. Xu, B. Q. Wei, W. C. H. Choy, *Adv. Opt. Mater.* **2015**, *3*, 1220.
[5] X. G. Ren, X. C. Li, W. C. H. Choy, *Nano Energy* **2015**, *17*, 187.
[6] W. R. Cao, J. G. Xue, *Energy Environ. Sci.* **2014**, *7*, 2123.
[7] X. F. Liu, B. Wu, Q. Zhang, J. N. Yip, G. N. Yu, Q. H. Xiong, N. Mathews, T. C. Sum, *ACS Nano* **2014**, *8*, 10101.
[8] B. Wu, X. Y. Wu, C. Guan, K. F. Tai, E. K. L. Yeow, H. J. Fan, N. Mathews, T. C. Sum, *Nat. Commun.* **2013**, *4*, 2004.
[9] J. Wang, Y. J. Lee, A. S. Chadha, J. Yi, M. L. Jespersen, J. J. Kelley, H. M. Nguyen, M. Nimmo, A. V. Malko, R. A. Vaia, W. D. Zhou, J. W. P. Hsu, *J. Phys. Chem. C* **2013**, *117*, 85.
[10] C. E. Petoukhoff, Z. Q. Shen, M. Jain, A. M. Chang, D. M. O'Carroll, *J. Photonics Energy* **2015**, *5*, 057002.
[11] J. B. You, X. H. Li, F. X. Xie, W. E. I. Sha, J. H. W. Kwong, G. Li, W. C. H. Choy, Y. Yang, *Adv. Energy Mater.* **2012**, *2*, 1203.
[12] H. A. Atwater, A. Polman, *Nat. Mater.* **2010**, *9*, 205.
[13] L. Y. Lu, Z. Q. Luo, T. Xu, L. P. Yu, *Nano Lett.* **2013**, *13*, 59.
[14] X. H. Li, W. C. H. Choy, H. F. Lu, W. E. I. Sha, A. H. P. Ho, *Adv. Funct. Mater.* **2013**, *23*, 2728.
[15] S. W. Baek, J. Noh, C. H. Lee, B. Kim, M. K. Seo, J. Y. Lee, *Sci. Rep.* **2013**, *3*, 1726.
[16] X. Yang, C. C. Chueh, C. Z. Li, H. L. Yip, P. P. Yin, H. Z. Chen, W. C. Chen, A. K. Y. Jen, *Adv. Energy Mater.* **2013**, *3*, 666.
[17] K. Yao, M. Salvador, C. C. Chueh, X. K. Xin, Y. X. Xu, D. W. deQuilettes, T. Hu, Y. W. Chen, D. S. Ginger, A. K. Y. Jen, *Adv. Energy Mater.* **2014**, *4*, 1400206.
[18] W. E. I. Sha, W. C. H. Choy, Y. G. Liu, W. C. Chew, *Appl. Phys. Lett.* **2011**, *99*, 113304.
[19] J. Yang, J. B. You, C. C. Chen, W. C. Hsu, H. R. Tan, X. W. Zhang, Z. R. Hong, Y. Yang, *ACS Nano* **2011**, *5*, 6210.
[20] G. Kakavelakis, E. Stratakis, E. Kymakis, *Chem. Commun.* **2014**, *50*, 5285.
[21] Y. S. Hsiao, S. Charan, F. Y. Wu, F. C. Chien, C. W. Chu, P. L. Chen, F. C. Chen, *J. Phys. Chem. C* **2012**, *116*, 20731.
[22] F. X. Xie, W. C. H. Choy, C. C. D. Wang, W. E. I. Sha, D. D. S. Fung, *Appl. Phys. Lett.* **2011**, *99*, 153304.
[23] C. C. D. Wang, W. C. H. Choy, C. H. Duan, D. D. S. Fung, W. E. I. Sha, F. X. Xie, F. Huang, Y. Cao, *J. Mater. Chem.* **2012**, *22*, 1206.
[24] X. H. Li, W. C. H. Choy, L. J. Huo, F. X. Xie, W. E. I. Sha, B. F. Ding, X. Guo, Y. F. Li, J. H. Hou, J. B. You, Y. Yang, *Adv. Mater.* **2012**, *24*, 3046.
[25] W. C. H. Choy, X. G. Ren, *IEEE J. Sel. Top. Quantum Electron.* **2016**, *22*, 1.
[26] W. E. I. Sha, X. H. Li, W. C. H. Choy, *Sci. Rep.* **2014**, *4*, 6236.
[27] W. E. I. Sha, H. L. Zhu, L. Z. Chen, W. C. Chew, W. C. H. Choy, *Sci. Rep.* **2015**, *5*, 8525.
[28] L. Shao, A. S. Susha, L. S. Cheung, T. K. Sau, A. L. Rogach, J. F. Wang, *Langmuir* **2012**, *28*, 8979.
[29] M. Chirumamilla, A. Gopalakrishnan, A. Toma, R. P. Zaccaria, R. Krahne, *Nanotechnology* **2014**, *25*, 235303.
[30] H. F. Lu, H. X. Zhang, S. Yu, S. W. Zeng, K. T. Yong, H. P. Ho, *Plasmonics* **2012**, *7*, 167.
[31] D. Kozanoglu, D. H. Apaydin, A. Cirpan, E. N. Esenturk, *Org. Electron.* **2013**, *14*, 1720.
[32] A. Ng, W. K. Yiu, Y. Foo, Q. Shen, A. Bejaoui, Y. Y. Zhao, H. C. Gokkaya, A. B. Djurisic, J. A. Zapien, W. K. Chan, C. Surya, *ACS Appl. Mater. Interfaces* **2014**, *6*, 20676.
[33] A. Taflove, S. Hagness, *Computational Electrodynamics: The Finite-Difference Time-Domain Method*, Artech House, Boston **2005**.
[34] X. G. Ren, Z. X. Huang, X. L. Wu, S. L. Lu, H. Wang, L. Wu, S. Li, *Comput. Phys. Commun.* **2012**, *183*, 1192.
[35] H. L. Yip, S. K. Hau, N. S. Baek, H. Ma, A. K. Y. Jen, *Adv. Mater.* **2008**, *20*, 2376.
[36] W. J. E. Beek, M. M. Wienk, M. Kemerink, X. N. Yang, R. A. J. Janssen, *J. Phys. Chem. B* **2005**, *109*, 9505.
[37] S. Chen, X. Y. Du, G. Ye, J. M. Cao, H. Sun, Z. Xiao, L. M. Ding, *J. Mater. Chem. A* **2013**, *1*, 11170.
[38] J. B. You, L. T. Dou, K. Yoshimura, T. Kato, K. Ohya, T. Moriarty, K. Emery, C. C. Chen, J. Gao, G. Li, Y. Yang, *Nat. Commun.* **2013**, *4*, 1446.
[39] A. M. Goodman, A. Rose, *J. Appl. Phys.* **1971**, *42*, 2823.

[40] S. Fabiano, S. Himmelberger, M. Drees, Z. H. Chen, R. M. Altamimi, A. Salleo, M. A. Loi, A. Facchetti, *Adv. Energy Mater.* **2014**, *4*, 1301409.

[41] G. F. Burkhard, E. T. Hoke, M. D. McGehee, *Adv. Mater.* **2010**, *22*, 3293.

[42] F. Fabregat-Santiago, G. Garcia-Belmonte, I. Mora-Sero, J. Bisquert, *Phys. Chem. Chem. Phys.* **2011**, *13*, 9083.

[43] G. Garcia-Belmonte, A. Guerrero, J. Bisquert, *J. Phys. Chem. Lett.* **2013**, *4*, 877.

[44] S. Trost, T. Becker, K. Zilberberg, A. Behrendt, A. Polywka, R. Heiderhoff, P. Gorrn, T. Riedl, *Sci. Rep.* **2015**, *5*, 7765.

[45] D. Zhang, W. C. H. Choy, F. X. Xie, W. E. I. Sha, X. C. Li, B. F. Ding, K. Zhang, F. Huang, Y. Cao, *Adv. Funct. Mater.* **2013**, *23*, 4255.

[46] F. X. Xie, W. C. H. Choy, W. E. I. Sha, D. Zhang, S. Q. Zhang, X. C. Li, C. W. Leung, J. H. Hou, *Energy Environ. Sci.* **2013**, *6*, 3372.

[47] N. Q. Yin, T. T. Jiang, J. Yu, J. W. He, X. Li, Q. P. Huang, L. Liu, X. L. Xu, L. X. Zhu, *J. Nanopart. Res.* **2014**, *16*, 2306.